

<https://doi.org/10.1038/s43247-025-02742-y>

Land aridification persists in vulnerable drylands under climate mitigation scenarios



Jinling Piao^{1,2}, Wen Chen^{3,4} , Jong-Seong Kug^{5,6} , Shangfeng Chen^{1,2}, Ji-Hoon Oh⁷,
Lin Wang^{1,2} & Qingyu Cai^{3,4}

Understanding how climate systems respond to carbon dioxide removal is crucial for assessing effectiveness of carbon neutrality policies. Here we show that rising carbon dioxide intensifies aridity over vast regions, particularly in vulnerable and climate-sensitive drylands based on idealized emission-driven simulations from an Earth System Model. Notably, even as carbon dioxide concentrations decline, arid regions continue to expand and experience worsening conditions, exacerbating climate injustice and resource conflicts. This pronounced hysteresis is primarily driven by long-lasting precipitation reductions in the tropics, linked to hysteresis of the intertropical convergence zone. The asymmetric response of arid zones suggests that reversing aridity intensification under global warming is exceptionally difficult. Further analysis highlights that negative carbon dioxide emissions may be essential to mitigating these deteriorating conditions, yet full recovery requires extended timescales. Our findings underscore irreversible risks of delayed action and stress the urgent need for carbon neutrality strategies that go beyond net-zero targets.

The intensification of the terrestrial water cycle has become one of the most substantial consequences of global warming, closely linked to a range of urgent challenges for both humans and the natural environment. These challenges include water scarcity, ecosystem degradation, and the resulting decline in land carbon storage capacities^{1–5}. From a global perspective, total precipitation (P) is projected to increase by 1 to 3% per degree of surface warming according to the atmospheric energy budget^{6–8}. However, this increase is counterbalanced by a rise in land evaporative demand measured as potential evapotranspiration (PET). This imbalance between moisture supply and demand is reflected in the declining Aridity Index (AI = P/PET, where both P and PET are based on annual total values) over recent decades^{9–12}, indicating worsening drying trends across many land areas^{13,14}.

Drylands cover nearly 47% of the global land area and are inhabited by more than one-third of the world's population¹⁵. A recent study highlights that climate model simulations have overestimated moisture availability over many arid and semiarid regions, failing to account for the increasing atmospheric demand, thereby amplifying concerns about an even drier

future for these vulnerable areas¹⁶. Such changes are expected to shift more global land areas toward drier climate types, leading to an expansion of drylands^{17–19}. Several model projections indicate that drylands could cover almost half of the global territory by the end of this century under a high emission scenario^{1,11,12}. Compared to a 1.5 °C warmer climate, a 4 °C warmer scenario would push an additional 11.2% of the continental area into drier types, exacerbating water scarcity and exposing more people to challenges such as severe droughts, land degradation, and desertification¹¹.

To mitigate global warming-related risks, including the increased terrestrial aridity, the 2015 Paris Agreement established a long-term goal of limiting global warming to well below 2 °C and preferably to 1.5 °C above the preindustrial level²⁰. Aiming at this target, many literatures have emphasized the need not only for conventional mitigation through reductions in CO₂ emissions but also for negative emissions via carbon dioxide removal (CDR) technologies^{21–25}. However, some studies have highlighted key challenges in deploying negative emissions technologies, including uncertainties about how natural land and ocean carbon sinks will respond to negative emissions^{23,26–28}. In particular, potential side effects are more likely

¹State Key Laboratory of Earth System Numerical Modeling and Application, Institute of Atmospheric Physics, Chinese Academy of Sciences, Beijing, China.

²Center for Monsoon System Research, Institute of Atmospheric Physics, Chinese Academy of Sciences, Beijing, China. ³Yunnan International Joint Laboratory of Monsoon and Climate Disasters/Department of Atmospheric Sciences, Yunnan University, Kunming, China. ⁴Yunnan Key Laboratory of Meteorological Disasters and Climate Resources in the Greater Mekong Subregion, Yunnan University, Kunming, China. ⁵School of Earth and Environmental Sciences, Seoul National University, Seoul, South Korea. ⁶Interdisciplinary Program in Artificial Intelligence, Seoul National University, Seoul, South Korea. ⁷Scripps Institution of Oceanography, University of California San Diego, La Jolla, CA, USA. ✉ e-mail: chenwen-dq@ynu.edu.cn; jskug@snu.ac.kr

to be detrimental to low-emitting communities, such as those in drylands, which are highly sensitive and vulnerable to rapid climate changes²⁶.

From this perspective, CDR-related pathways have been extensively evaluated from various perspectives with a key focus on the reversibility and hysteresis of climate responses^{24,29–34}. Both global mean precipitation and temperature have been suggested to be generally reversible to CO₂ changes, but exhibit hysteresis characteristics at regional scales^{35–38}. This naturally raises a critical question: Is global warming-induced drying in drylands reversible? If so, how rapidly can aridity recover in these regions under various climate mitigation scenarios? Furthermore, what physical processes govern the resilience of dryland aridity?

To address these issues, idealized emission-driven simulations were conducted under two scenarios: net-zero (Exp_zero) and negative emissions (Exp_neg) (see Methods and Fig. 1a). We analyzed changes in aridity intensity across the global territory during the ramp-up, ramp-down, and recovery phases of CO₂ concentrations, with a particular focus on differences between various climate zones. Our findings indicate that global warming exacerbates arid conditions across vast regions worldwide, significantly intensifying dryness threats in already arid areas. These arid lands continue to grow drier and expand even when CO₂ levels decline, presenting a formidable challenge to reversing the worsening aridity. Further analysis suggests that negative emissions may be necessary to alleviate these aggravated aridity conditions caused by global warming.

Results

Terrestrial aridity changes with consistent CO₂ increase

During the ramp-up period, rising CO₂ concentrations gradually increase terrestrial near-surface air temperature (SAT) from the initial state to its peak (Fig. 1a, b). This warming further intensifies the hydrological cycle^{39–41}, resulting in an upward tendency in both the global mean precipitation and PET amount (Fig. 1b). However, because land warms more quickly than the oceans, the humidity of the incoming air originating from oceans does not rise enough to maintain constant relative humidity, leading to an overall decline across the global territory^{42,43}. As a result, the saturation deficit—the difference between actual and saturation water vapor content, which is a key driver of PET, increases at a much faster rate than precipitation^{9,42–44}. This is reflected in the continuous AI decline (Fig. 1c), pointing to a general intensification of aridity in a warming world.

By the time CO₂ concentrations peak (MAX, 2093–2122), the global terrestrial mean precipitation and PET amount also reach local maxima (Fig. 1b). The PET's dominant effects for the aridity result in the most severe drying conditions for the entire simulation period (Fig. 1c). In general, precipitation responses exhibit a heterogeneous spatial pattern with increases concentrated in mid-to-high latitudes and decreases in the tropics (Supplementary Fig. 1b). Global warming intensifies precipitation in mid-to-high latitudes due to increased atmospheric moisture and a poleward shift of storm tracks^{45,46}. In contrast, drying emerges over subtropical drylands such as North Africa, driven by an expanding Hadley circulation^{47,48}, and across tropical monsoon regions in North and South America where a weakened Walker circulation suppresses convection^{49,50}. However, the widespread PET increases driven by warming outpace the precipitation gains in mid-to-high latitudes, leading to significant AI drops over most of the global territory (Supplementary Fig. 1). Notably, the most remarkable AI drops are concentrated over the tropical arid zones, indicating an even drier future for those drylands, as consistently demonstrated in previous studies^{1,16,51}.

Terrestrial aridity response to net-zero and negative CO₂ emissions

After the peak, the emission pathways start to diverge in these two scenario experiments. Under Exp_zero, the atmospheric CO₂ concentration declines steadily with the onset of the zero emissions (Fig. 1a). Correspondingly, the global terrestrial mean SAT decreases until around 2250 but then rises slightly and ultimately remains above the initial state (Fig. 1b). Several simulations have suggested that the Atlantic Meridional Overturning Circulation (AMOC) plays a critical role in this SAT overshoot: while AMOC

weakens in response to the increasing CO₂, it gradually strengthens during the decreasing period with the partial recovery of the northward heat transport, contributing to the subsequent SAT increase^{29,52–54}. Regarding this SAT overshoot, several studies have reported a spread in model behaviour following the cessation of emissions, highlighting the warming effects of reduced ocean heat uptake—though these are partly offset by continued carbon uptake by the ocean and terrestrial biosphere^{25,55}. Additionally, deep-ocean warming induces a sea surface temperature (SST) anomaly pattern that further contributes to the SAT overshoot³⁰. The precipitation and PET show fairly in-phase variations with the SAT, featuring a decreasing and then increasing tendency (Fig. 1b). These combined impacts lead to a modest AI increase by the end of Exp_zero (Fig. 1c).

In the Exp_neg scenario, the SAT shows a sharp decline after the CO₂ peak, coinciding with a steep drop in atmospheric CO₂ concentration. However, it quickly transitions into a rising phase during the restoring period (RS, 2301–2400), despite the subsequent zero emissions (Fig. 1a, b). This rebound is closely related to the more rapid recovery of the AMOC compared to that in Exp_zero (Fig. 1c). Following the CO₂ peak, both the precipitation and PET experience an abrupt decline in the course of the CO₂ ramp-down, then reversing to an increasing tendency once the zero CO₂ emissions begin (Fig. 1b). During the ramp-down phase, the PET responds faster than precipitation to the decreasing CO₂ concentrations as is in the ramp-up case, thereby alleviating the global terrestrial aridity conditions indicated by a sharp increase in AI (Fig. 1c). Under subsequent zero emissions, the precipitation increase accelerates in association with the AMOC's recovery. Nevertheless, the recovery remains stagnant, failing to restore the AI to its original state (Fig. 1c).

It is worth noting that despite the approximately linear response of both precipitation and PET to CO₂ forcing, the ramp-down phase is characterized by relatively lower precipitation and higher PET compared to the ramp-up phase, even at equivalent CO₂ concentrations. These combined effects result in a drier climate characterized by lower AIs as CO₂ declines, highlighting a general hysteresis in the terrestrial mean aridity response.

Hysteresis of terrestrial aridity to CO₂ forcing

Given the notable differences in climate sensitivities across various climate zones, we will next explore the aridity response for specific climate sub-types (Supplementary Fig. 2), focusing on hysteresis and reversibility characteristics. Notable diversities exist in the aridity response across different climate zones, with the arid zone exhibiting unique characteristics compared to others (Fig. 2). Both precipitation and AI in the arid zone demonstrate distinctive behaviors during the ramp-up and ramp-down phases (Fig. 2a, e). Although precipitation initially increases during the ramp-up, consistent with the global-average trend, it subsequently declines, and this decline becomes more pronounced during the ramp-down phase (Fig. 2e). Meanwhile, the PET shows a relatively weak hysteresis feature, and its overall magnitude remains higher during the ramp-down phase (Fig. 2f). These factors together result in a dramatic AI decline during the ramp-up phase, which continues during the ramp-down phase but at a slower rate, revealing a consistently worsening aridity for the arid zone (Fig. 2a). In accompany with this distinctive AI hysteresis, the corresponding area of the arid zone expands sharply during the ramp-up, and this expansion consists until the latter half of the ramp-down phase, also featuring an apparent hysteresis behavior (Fig. 1c). This behavior contrasts sharply with the minimal changes in arid zone area under the Exp_zero scenario following zero emissions.

In comparison, other climate zones show roughly linear hydrological response to CO₂ forcing, but all are subject to drier climates in the ramp-down period similar to the global terrestrial mean (Fig. 2b–d and Supplementary Fig. 4). The semiarid zone shows a sharp reduction in area once CO₂ emissions decrease, eventually shrinking below its initial extent. Meanwhile, the dry subhumid and humid zones display a more symmetric response to CO₂ forcing (Supplementary Fig. 3). It is worth noting that even slight AI changes can trigger severe aridity issues, given the narrow AI range used to define climate categories. These findings highlight that even if CO₂ levels are restored to their original levels, the amplified aridity caused by

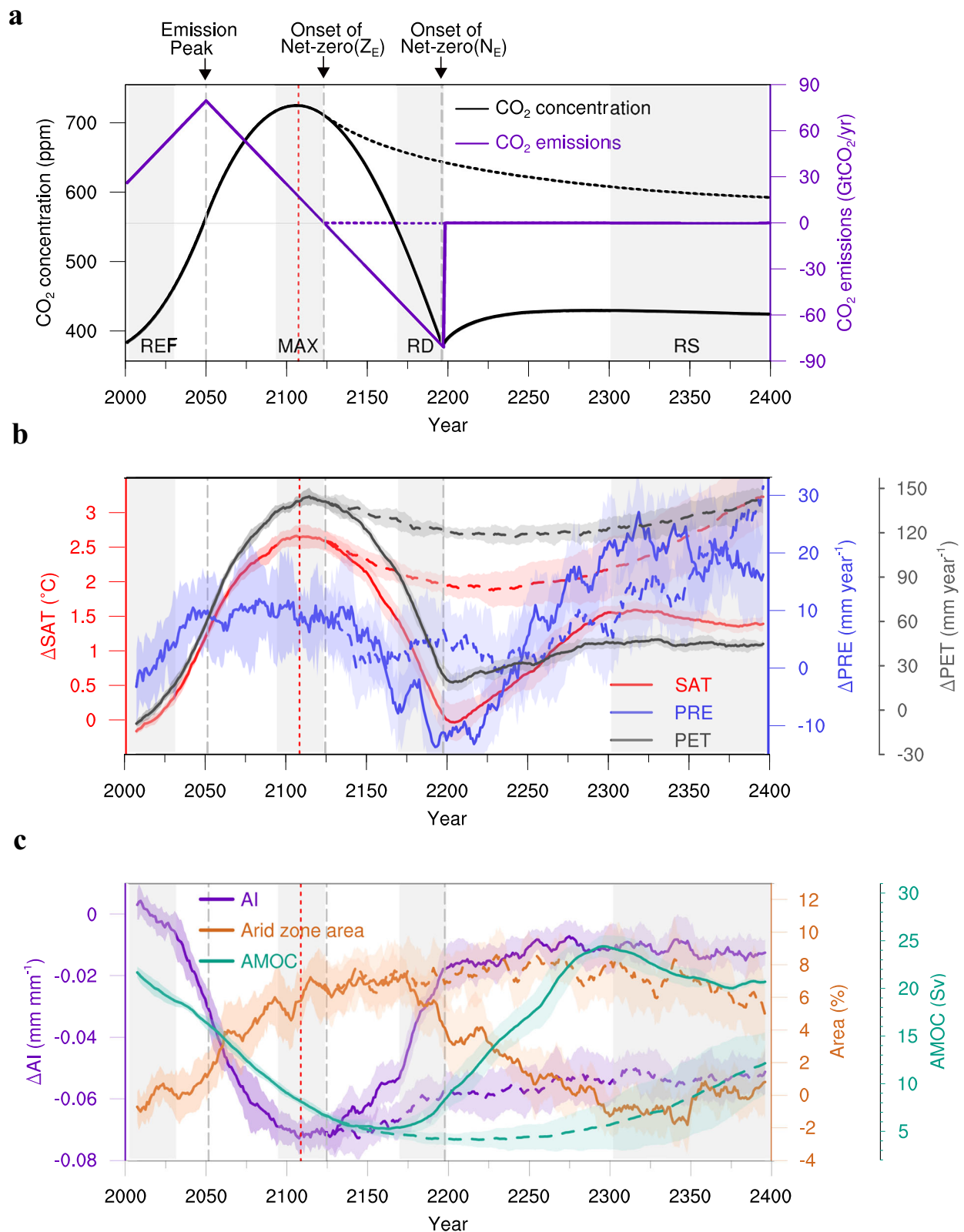


Fig. 1 | Temporal evolution of temperature, precipitation, and aridity index (AI) in idealized net-zero (Z_E) and negative emissions (N_E) scenarios. **a** Time series of atmospheric CO₂ concentration (black lines) and anthropogenic CO₂ emissions (purple lines) under Z_E (dashed lines) and N_E (solid lines). The four gray boxes denote key phases: 2001–2030 (reference period, REF), 2093–2122 (CO₂ peak phase, MAX), 2168–2197 (late CO₂ ramp-down phase, RD), and 2301–2400 (restoring period, RS), respectively. **b–c** Time series of the global terrestrial average surface air temperature (SAT; red lines), precipitation (PRE; blue lines) and potential evapotranspiration (PET; gray

lines) (b), AI (purple lines), areal coverage of the arid zone (percentage of the mean arid area during the REF period; orange lines) and the Atlantic Meridional Overturning Circulation (AMOC) strength (green lines) (c). The AMOC strength is defined as the average of the annual mean Atlantic meridional ocean stream function within 35–45°N at a depth of 1000 m. All lines depict annual means smoothed with an 11-year running mean. Thick lines and shading indicate ensemble means and the corresponding ensemble standard deviation ($\pm 1\sigma$) range, respectively. SAT, PRE, PET, and AI are shown as anomalies relative to the REF period.

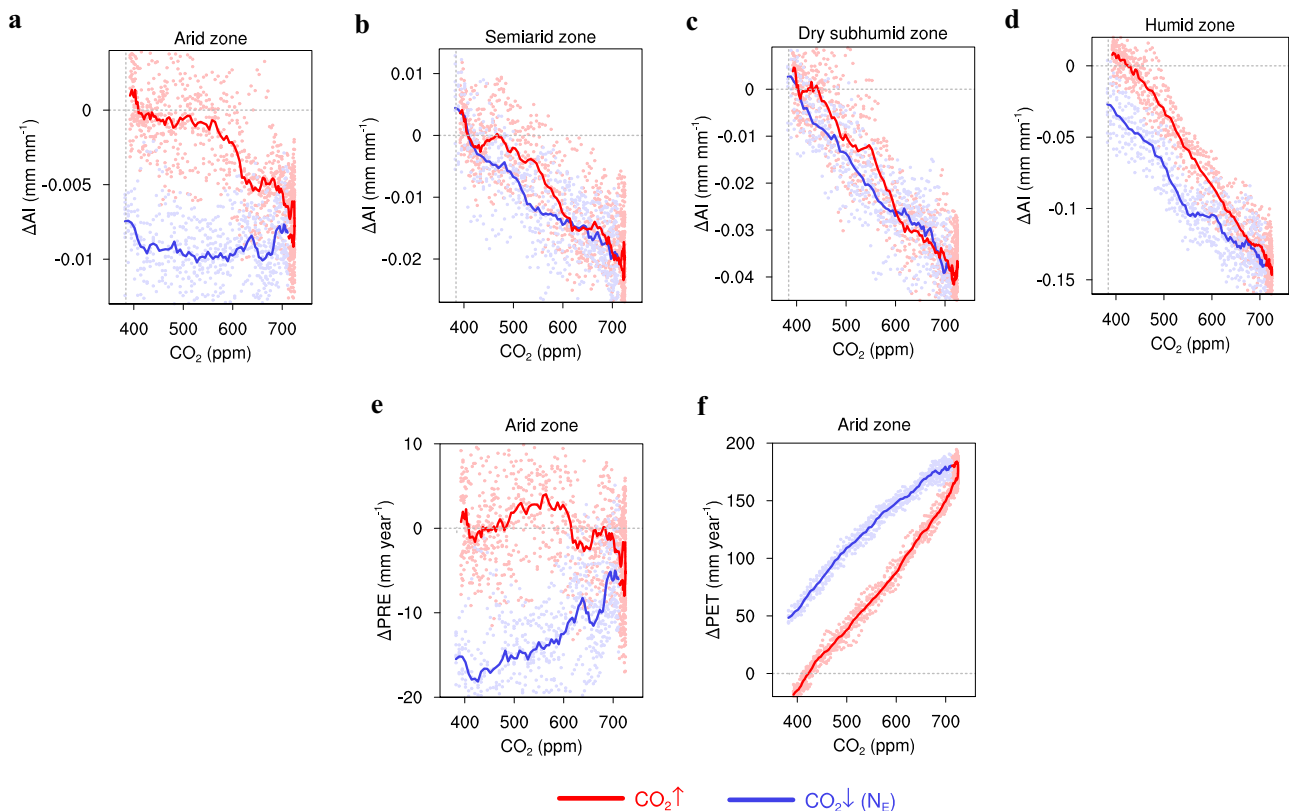


Fig. 2 | Evolution and hysteresis of AI across different climate zones.

a–d Hysteresis of the domain-averaged AI anomalies relative to the REF period (2001–2030) corresponding to the CO_2 concentration in the arid (a), semiarid (b), dry subhumid (c) and humid (d) zones. **e, f** The same as (a), but for precipitation (e) and PET (f) in the arid zone, respectively. All calculations were performed after

applying the 11-year running mean. Lines and dots indicate ensemble mean and ensemble spread, respectively, with the same colors representing one specific period in regard to the CO_2 evolution (red: increasing CO_2 period; blue: decreasing CO_2 period in Exp_neg (N_E)).

global warming may not be fully reversed, posing a particular threat to arid regions plagued by long-term water scarcity issues.

To emphasize this hysteresis behavior, we further examined the differences in the response pattern between the late ramp-down (RD, 2168–2197) and the reference period (REF, 2001–2030), both of which are characterized by the same CO_2 levels (Fig. 3). During the late ramp-down, the tropics and extensive high-latitude regions in the Northern Hemisphere experience reduced precipitation but increased PET (Fig. 3b, c), and thus are subject to more severe aridity issues compared to the REF period (Fig. 3a). The enhanced PET in the far north is likely associated with Arctic amplification, which intensifies warming and surface energy fluxes in the region⁵⁶. In contrast, regions in North and South America show increased precipitation and reduced PET (Fig. 3b, c), collectively alleviating local aridity conditions (Fig. 3a). Consistent with the pronounced hysteresis behavior observed in the arid zone, the exemplified aridity issues in the ramp-down period, together with reduced precipitation show the most remarkable signals across widespread arid zones in the tropics (Fig. 3a). Notably, similar precipitation responses are consistently identified in model simulations from the sixth phase of the Coupled Model Intercomparison Project, further reinforcing the reliability and robustness of our results^{57–59}.

This widespread drying pattern in the tropics is closely related to the hysteresis in the latitudinal displacement of the intertropical convergence zone (ITCZ) in response to CO_2 forcing^{29,60,61}. We tracked the ITCZ's latitudinal shift using the precipitation centroid index (P_{cent}), which represents the median zonal-mean precipitation in the tropics^{62–64} (Methods). The ITCZ remains stable until 2050, after which it gradually shifts southward and eventually settles in the Southern Hemisphere by the end of the ramp-down phase (Supplementary Fig. 5). This shift contributes to widespread drying in the tropics (Fig. 3a, b)^{29,61,65}. The hysteresis in the ITCZ is closely related to the

distribution of tropospheric temperatures in the tropics^{29,60}, which influence the ITCZ's movement by modulating the cross-equatorial energy flux^{19,66,67}.

Currently, the Northern Hemisphere (NH) is warmer due to factors such as land–ocean asymmetry, Antarctic cooling, and northward heat transport via the AMOC⁶⁸. Within the tropics (30°S–30°N), the temperature contrast fluctuates slightly in the early ramp-up phase before 2050, but begins to decline thereafter, continuing until the end of the ramp-down (Supplementary Fig. 5a). During the ramp-up, the weakening AMOC contributes to this process by reducing northward heat transport, which offsets the faster warming in the NH tropics during the early decades and gradually dominates the decrease in the interhemispheric temperature contrast after 2050. In the ramp-down phase, the temperature contrast continues to shrink (Supplementary Fig. 5a), mainly attributed to the ongoing AMOC weakening and delayed cooling in the Southern Ocean^{29,60,61}. This shift in hemispheric temperature contrasts closely tracks changes in P_{cent} , further supporting its connection to the ITCZ's hysteresis response.

This ITCZ hysteresis has profound impacts on the global hydrological cycle, intensifying drying conditions in the tropics (Fig. 3a, b)^{29,61,65}. In this context, the arid zone for the RD period expands by nearly 6% relative to the REF baseline (Fig. 1c). This exacerbates the potential crisis of land degradation and desertification. The even drier climate and more widespread coverage of arid regions are particularly concerning, given the fragile ecological environments in these areas that are highly sensitive to fluctuations in dry and wet conditions^{69–71}.

Reversibility of amplified terrestrial aridity under negative emissions

To investigate whether the exemplified aridity driven by global warming could revert to the initial state, changes in the RS period are further

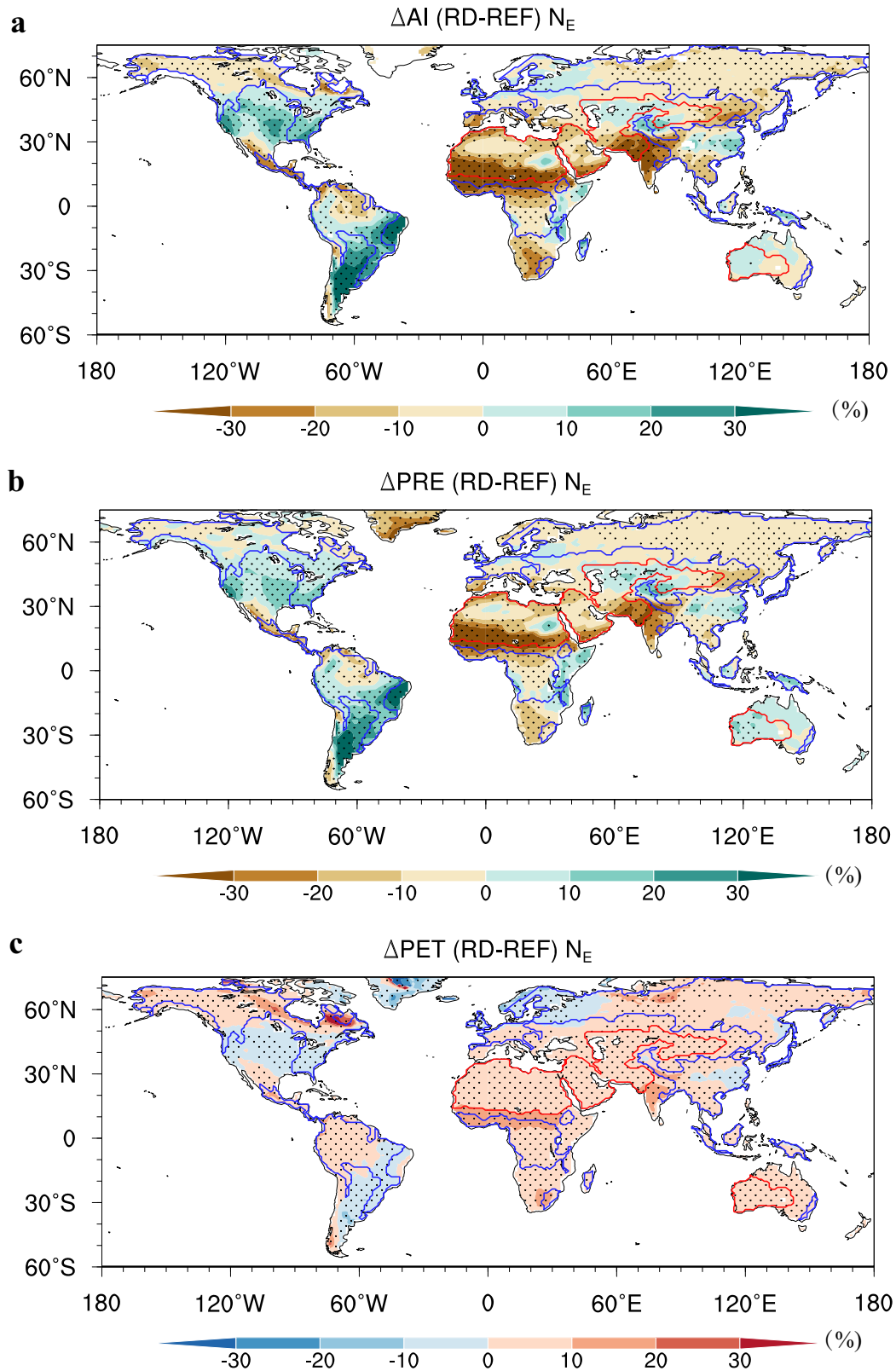


Fig. 3 | Hysteresis of the global terrestrial hydrological cycle. a–c Differences in the terrestrial AI (a), precipitation (b), and PET (c) between RD (2168–2197) and REF (2001–2030) in N_E for the ensemble mean. The differences are presented as percentage anomalies relative to the REF period. All calculations were performed after applying an 11-year running mean. Regions enclosed by red and blue lines represent

the climatological mean domains of the arid and humid zones for REF, respectively. The dotted areas are where the ensemble mean results exceed the 95% confidence threshold based on a two-tailed Student's *t*-test. Statistically significant results are corrected for false discovery rate (FDR; $\alpha FDR = 0.1$; Methods).

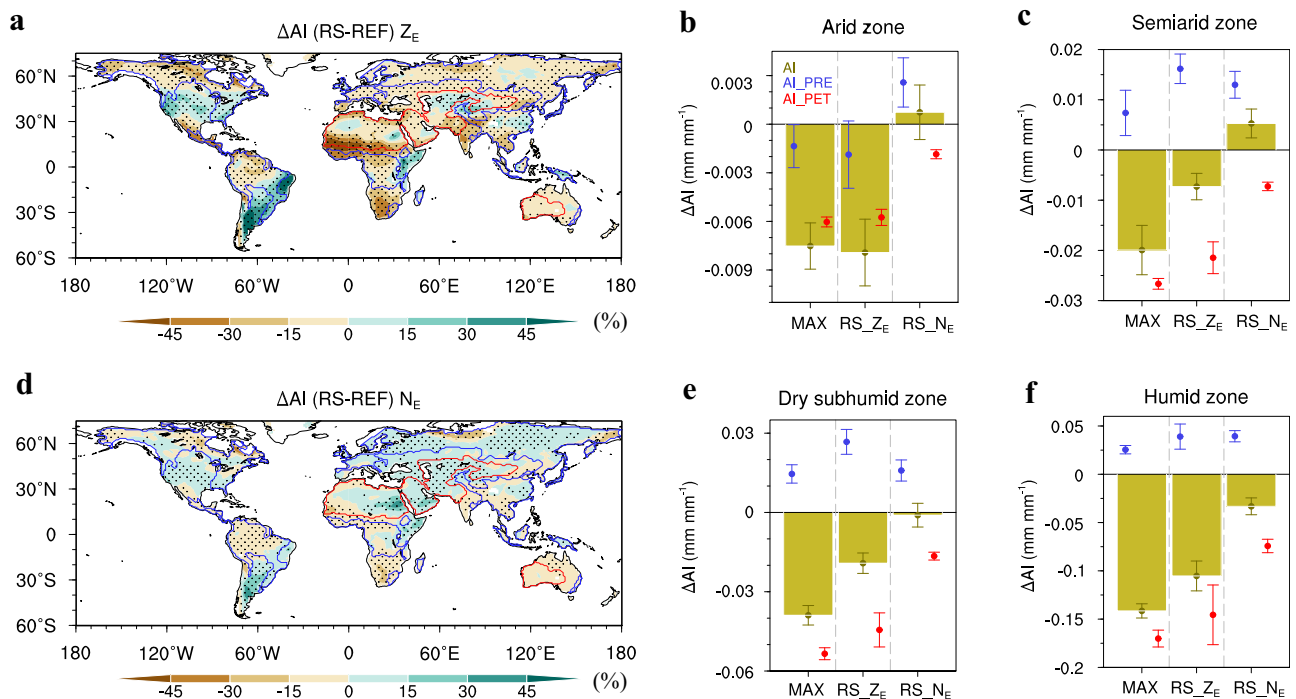


Fig. 4 | Changes in the global terrestrial hydrological cycle under net-zero and negative emissions. a, d Changes in the global terrestrial AI in the RS period under Z_E (a) and N_E (d) for the ensemble mean. Dots indicating changes significant at the 95% confidence level based on a two-tailed Student's *t*-test, with corrections for the FDR ($\alpha\text{FDR} = 0.1$; Methods). **b, c, e, f** Ensemble mean changes in the regional average AI (bars), AI dominated by precipitation (AI_PRE) (blue dots), AI

dominated by PET (red dots) during MAX (2093–2122), RS (2301–2400) under net-zero (RS_Z_E) and negative emissions (RS_N_E) for arid (b), semiarid (c), dry subhumid (e) and humid zones (f), respectively. All calculations were performed after applying the 11-year running mean. Whiskers around dots represent ±1 standard deviation of the corresponding model spread. Changes in (a) and (d) are presented as percentage anomalies relative to the REF period (2001–2030).

examined under the two emission pathways. Under Exp_zero, the AI shows similar patterns to those in the MAX period with domain-wide deterioration in aridity conditions (Fig. 4a). Under these circumstances, all the involved climate zones are subject to more severe aridity issues compared to the REF period (Fig. 4b, c, e, f). Notably, following the CO₂ peak, the precipitation in the tropical arid regions north of the equator declines further due to the continuous southward shift of the ITCZ²⁹, as opposed to the increasing signals observed in other regions (Supplementary Fig. 6c). Meanwhile, PET exhibits increasing trends in the tropical arid regions near the equator and in southern Africa, in contrast to the widespread decreases across the Northern Hemisphere (Supplementary Fig. 6e). In this context, the overall aridity of these arid zones intensifies further, even surpassing the conditions observed during the MAX period under this scenario (Supplementary Fig. 6a). Additionally, the extent of the arid zone also remains comparable to that of the MAX period (Fig. 1c). For other climate zones, though the AI increases to varying extents after the CO₂ peak, the aridity conditions remain worse than during the REF period (Fig. 4a). These findings highlight the limited effectiveness of the zero emissions in mitigating global terrestrial aridity, and underscore the potential for adverse impacts on arid regions already grappling with long-term water scarcity crises.

In terms of the RS period of Exp_neg, the areal coverage of drier-than-initial conditions sharply decreases by nearly 24% compared to Exp_zero (Fig. 4d). At this stage, the hydrological response exhibits spatially consistent features: higher-than-initial PET dominates most global land areas, accompanied by widespread precipitation increases (Supplementary Fig. 7b, d). Exceptions to this pattern include localized precipitation decreases over the equatorial tropics, South Africa, and Australia. In the northern hemisphere, precipitation increases generally exceed those of PET, resulting in extensive aridity conditions significantly improved beyond the initial state (Fig. 4d). In contrast, much of the Southern Hemisphere experiences a combination of precipitation decreases and PET increases, which together

impede recovery to the initial state. Compared to the MAX period, the intensified aridity conditions during the RS period are broadly alleviated, primarily due to the combined effects of increased precipitation and reduced PET (Supplementary Fig. 6b, d, f).

Note that under Exp_neg, most climatologically drylands (i.e., arid, semiarid, and dry sub-humid zones) appear to eventually return to or even surpass their initial wetness levels. This even includes tropical arid regions that exhibit pronounced aridity hysteresis under CO₂ forcing (Fig. 4d), with the corresponding extent eventually reversed back to the initial level (Fig. 1c). Analyzing aridity trends within specific climate zones provides deeper insights into this phenomenon. In arid and semiarid zones, precipitation increases outpace the rise in PET, facilitating a transition to overall wetter-than-initial conditions in these climate-sensitive and ecologically vulnerable areas (Fig. 4b, c). In the dry subhumid zone, precipitation and PET ultimately increase at roughly comparable rates, sustaining conditions close to the initial state (Fig. 4e). By contrast, in the humid zone, precipitation gains are eventually counterbalanced by rising PET, preventing recovery to the initial state (Fig. 4f). These findings highlight a clear difference between the two emission scenarios. While net-zero emissions may stabilize CO₂ levels, they are insufficient to reverse aridification, especially in regions facing long-term water stress. In contrast, negative emissions not only slow further drying but also help restore past losses, offering a more effective path to recover hydrological balance and strengthen climate resilience.

Discussion

It has been well documented that global warming substantially affects terrestrial aridity, particularly in drylands with vulnerable ecosystems that rely heavily on dry-wet conditions^{1,3,19}. In recent decades, persistent warming driven by greenhouse gas emissions has profoundly altered regional water cycles in these climate-sensitive areas, even triggering tipping points that could push local climates into potentially irreversible states¹⁹. Given these

potential detrimental consequences, the reversibility and hysteresis have received increasing attention and have already become hotspots in climate change research.

In this study, we mainly utilized two idealized emission-driven simulations to compare the aridity response to CO₂ forcing across different climate zones. Consistent with previous studies, the increasing CO₂ leads to a significant deterioration in aridity conditions for the widespread land surface, with the most pronounced signals concentrated over the already dry lands. In particular, the arid zone consistently expands and experiences worsening aridity even in the ramp-down phase, featuring a remarkable hysteresis behavior. This is mainly due to the hysteresis behavior of the ITCZ, which leads to sustained precipitation decreases over widespread tropical arid regions as CO₂ ramps up and ramps down, resulting in aridity hysteresis²⁷. Though other climate zones show relatively weak hysteresis, their aridity conditions are generally amplified during ramp-down compared to ramp-up. These results together highlight that the worsening aridity driven by global warming might not be fully recovered even when the CO₂ returns to its initial state. In particular, the recovery is highly challenging for arid zones struggling with long-term water scarcity issues, where strong hysteresis exists concerning the aridity response.

In order to examine whether the worsening aridity could eventually revert to initial conditions, we further examined the restoring period under the two emission scenarios. Our findings indicate that although net-zero emissions may stabilize atmospheric CO₂, aridity may still intensify in arid regions as a consequence of the lingering effects of past high emissions. In contrast, negative emissions demonstrate significant potential to mitigate aridity issues over widespread areas, particularly in arid and semiarid regions. These results suggest that achieving net-zero emissions alone may be insufficient to mitigate worsening aridity driven by global warming, while additional carbon removal measures could offer more substantial benefits, albeit requiring an extended period for full recovery.

Our findings underscore the pronounced hysteresis of aridity within dry zones, distinguishing it from the relatively more responsive dynamics of mean temperature and precipitation. This difference highlights the deep-rooted persistence of arid conditions, even under shifting climatic baselines. Such damage may far exceed prior estimations, as the slow recovery of arid ecosystems further amplifies vulnerabilities. While model projections indicate that negative emissions could potentially reverse aridity changes, the timescales required are likely to span decades, during which substantial and potentially irreversible ecosystem degradation may occur. These insights emphasize the cascading effects of delayed action in climate mitigation, where the consequences of inaction become increasingly irreversible over time. Given the narrowing window of opportunity to avert the worst outcomes, our study strongly suggests that immediate and decisive efforts to reduce greenhouse gas emissions are critical to minimizing the risks associated with long-term aridity and ecosystem degradation.

Methods

Datasets and experimental design

To examine the response of the global terrestrial aridity to net-zero and negative CO₂ emissions, we utilized the Community Earth System Model 2 (CESM2) to conduct idealized emission-driven simulations. CESM2 integrates multiple components: the atmosphere (The Community Atmosphere Model version 6, CAM6), ocean (The Parallel Ocean Program version 2, POP2)^{72,73}, sea ice (The Community Ice Code version 5, CICE5)⁷⁴, and land models (The Community Land Model version 5, CLM5)⁷². Both the CAM6 and CLM5 share a horizontal resolution of ~1° with 32 vertical levels, while POP2 and CICE5 operate at a nominal 1° horizontal resolution (meridional resolution ~0.27° near the equator) and 60 vertical ocean levels. The CLM5 features terrestrial carbon and hydrological cycles, while the Marine Biogeochemistry Library characterizes ocean carbon cycles in CESM2⁷⁵.

With the assumption of gradual emission reductions enabled by CDR technologies, we conducted two idealized emission-driven simulations—Exp_zero and Exp_neg—to ensure the continuity and feasibility of CO₂ emission pathways. During the positive emission phase (2000–2050) in both

experiments, anthropogenic CO₂ emissions increase at a similar rate to the SSP5-8.5 scenario trajectory (1.09 GtCO₂ increase per year). Emissions then decline at the same rate until 2123 (~1500 Pg C of total cumulative emissions). After that, the pathways diverge: in Exp_zero, zero CO₂ emissions are maintained through the end of the simulation; in Exp_neg, CO₂ emissions continue to decline at the same rate until atmospheric CO₂ returns to its initial level (~383 ppm) by 2197, after which emissions are held at zero (Fig. 1a).

Under the emission-driven experiment design, atmospheric CO₂ concentrations in the model are shaped not only by prescribed anthropogenic emissions but also by the responses of terrestrial and oceanic carbon sinks. In this study, atmospheric CO₂ reaches a peak around the year 2107, when anthropogenic emissions are effectively balanced by natural carbon uptake. Thereafter, CO₂ levels gradually decline, sustained by continued net uptake by land and ocean carbon sinks⁷⁶. For non-CO₂ conditions, such as land use and greenhouse gas forcings other than CO₂, they are held constant at their year 2000 level. To account for uncertainty, we employ nine ensemble members initialized with slightly different initial states.

Furthermore, we used observational datasets to assess the models' performance in simulating climatological aridity conditions globally. Specifically, we utilized monthly mean precipitation and PET data from the Climatic Research Unit (CRU TS v. 4.08), with a horizontal resolution of 0.5°⁷⁷. Overall, the ensemble mean of the models effectively reproduces the key characteristics of the observed geographic distribution of aridity conditions (Supplementary Fig. 2).

Definition of indices

We first calculated PET using the widely-used Penman-Monteith algorithm^{1,4,13,78,79}. This method incorporates multiple variables closely related to the evaporative process, including net radiation, relative humidity, wind speed, temperature, and vegetation characteristics. Subsequently, we used the AI—the ratio of annual precipitation to PET—to evaluate terrestrial aridity degrees^{1,9,12}. The AI reflects the balance between moisture supply and demand and is commonly employed to classify land surfaces into distinct categories based on dryness and wetness: arid (AI < 0.2), semiarid (0.2 ≤ AI < 0.5), dry subhumid (0.5 ≤ AI < 0.65) and humid (AI ≥ 0.65) zones^{1,80}. The first three categories with AI smaller than 0.65 are typically considered drylands^{12,81,82}.

For a given region, lower AI values indicate drier climates, while higher values correspond to more humid conditions. Although the AI is a dimensionless index, small changes in its value can have distinct ecological and hydrological implications depending on the baseline aridity level of a region^{1,11,12}. This highlights the importance of interpreting AI anomalies in conjunction with their baseline climatic context and zonal classification. This quantitative index is particularly effective for tracking long-term shifts in aridity and persistent drought conditions^{1,83,84}.

To better quantify the relative contributions of precipitation and PET to changes in AI, we calculated two additional indices: AI_PRE and AI_PET. These indices isolate the impact of each variable on AI evolution. AI_PRE represents the AI evolution driven solely by precipitation, with PET held constant at its mean value from the REF period. Conversely, AI_PET reflects AI changes driven solely by PET, with precipitation fixed at its REF period mean. This approach provides a clearer understanding of how each factor individually influences aridity dynamics.

The precipitation centroid is calculated as the median latitude where the annual zonal-mean precipitation in the tropics (from 20°S to 20°N) is evenly divided^{62–64}. To improve the resolution of the centroid, the precipitation data are interpolated onto a 0.1° grid over the tropical region, allowing for more precise determination at smaller intervals than the original grid spacing.

Statistical significance testing

We primarily employed the 9-member ensemble mean to identify spatial differences across multiple time periods under the emission-driven experiments. The significance of these differences was assessed using a

two-tailed Student's t test. To mitigate potential spurious significance arising from spatial autocorrelation, we applied the Benjamini–Hochberg false discovery rate (FDR) correction ($\alpha\text{FDR} = 0.1$)⁸⁵, which corresponds to a global significance level of $\alpha = 0.05$ ⁸⁶.

Data availability

The processed data and code used to generate the results in this study are available in the Zenodo database (<https://doi.org/10.5281/zenodo.15872988>)⁸⁷.

Code availability

Custom codes used for constructing all the figures are available in the Zenodo database (<https://doi.org/10.5281/zenodo.15872988>).

Received: 18 April 2025; Accepted: 22 August 2025;

Published online: 02 September 2025

References

- Huang, J., Yu, H., Guan, X., Wang, G. & Guo, R. Accelerated dryland expansion under climate change. *Nat. Clim. Chang.* **6**, 166–171 (2016).
- Donat, M. G., Lowry, A. L., Alexander, L. V., O’Gorman, P. A. & Maher, N. More extreme precipitation in the world’s dry and wet regions. *Nat. Clim. Chang.* **6**, 508–513 (2016).
- Trenberth, K. E. et al. Global warming and changes in drought. *Nat. Clim. Chang.* **4**, 17–22 (2014).
- Chiang, F., Mazdiyasni, O. & AghaKouchak, A. Evidence of anthropogenic impacts on global drought frequency, duration, and intensity. *Nat. Commun.* **12**, 2754 (2021).
- Fung, I. Y., Doney, S. C., Lindsay, K. & John, J. Evolution of carbon sinks in a changing climate. *Proc. Natl Acad. Sci. USA*. **102**, 11201–11206 (2005).
- Zhang, W. et al. Increasing precipitation variability on daily-to-multiyear time scales in a warmer world. *Sci. Adv.* **7**, eabf8021 (2021).
- Held, I. M. & Soden, B. J. Robust responses of the hydrological cycle to global warming. *J. Clim.* **19**, 5686–5699 (2006).
- Allen, M. R. & Ingram, W. J. Constraints on future changes in climate and the hydrologic cycle. *Nature* **419**, 224–232 (2002).
- Sherwood, S. & Fu, Q. A drier future?. *Science* **343**, 737–739 (2014).
- Chai, R. et al. Human-caused long-term changes in global aridity. *npj Clim. Atmos. Sci.* **4**, 65 (2021).
- Koutroulis, A. G. Dryland changes under different levels of global warming. *Sci. Total Environ.* **655**, 482–511 (2019).
- Feng, S. & Fu, Q. Expansion of global drylands under a warming climate. *Atmos. Chem. Phys.* **13**, 10081–10094 (2013).
- Dai, A. Increasing drought under global warming in observations and models. *Nat. Clim. Chang.* **3**, 52–58 (2013).
- Hessl, A. E. et al. Past and future drought in Mongolia. *Sci. Adv.* **4**, e1701832 (2018).
- Michael, C. et al. *World Atlas of Desertification* (European Commission, 2018).
- Allan, R. P. & Douville, H. An even drier future for the arid lands. *Proc. Natl Acad. Sci. USA*. **121**, e2320840121 (2024).
- Daliakopoulos, I. et al. The threat of soil salinity: A European scale review. *Sci. Total Environ.* **573**, 727–739 (2016).
- Greve, P. et al. Global assessment of trends in wetting and drying over land. *Nat. Geosci.* **7**, 716–721 (2014).
- Williams, A. P. et al. Forest responses to increasing aridity and warmth in the southwestern United States. *Proc. Natl Acad. Sci. USA* **107**, 21289–21294 (2010).
- UNFCCC. *Adoption of the Paris agreement, 21st Conference of the Parties* United Nations, (2015).
- Gasser, T., Guivarch, C., Tachiiri, K., Jones, C. D. & Ciais, P. Negative emissions physically needed to keep global warming below 2. °C. *Nat. Commun.* **6**, 7958 (2015).
- Kriegler, E. et al. Pathways limiting warming to 1.5 °C: a tale of turning around in no time?. *Philos. Trans. Roy. Soc. A: Math. Phys. Eng. Sci.* **376**, 20160457 (2018).
- MacDougall, A. H. Reversing climate warming by artificial atmospheric carbon-dioxide removal: Can a Holocene-like climate be restored?. *Geophys. Res. Lett.* **40**, 5480–5485 (2013).
- Jayakrishnan, K., Bala, G. & Caldeira, K. Dependence of climate and carbon cycle response in net zero emission pathways on the magnitude and duration of positive and negative emission pulses. *Earth’s Future* **12**, e2024EF004891 (2024).
- MacDougall, A. H. et al. Is there warming in the pipeline? A multi-model analysis of the Zero Emissions Commitment from CO₂. *Biogeosciences* **17**, 2987–3016 (2020).
- Anderson, K. & Peters, G. The trouble with negative emissions. *Science* **354**, 182–183 (2016).
- Fuss, S. et al. Negative emissions—Part 2: Costs, potentials and side effects. *Environ. Res. Lett.* **13**, 063002 (2018).
- Jones, C. D. et al. Simulating the Earth system response to negative emissions. *Environ. Res. Lett.* **11**, 095012 (2016).
- Kug, J.-S. et al. Hysteresis of the intertropical convergence zone to CO₂ forcing. *Nat. Clim. Change*. **12**, 47–53 (2022).
- Oh, J.-H. et al. Emergent climate change patterns originating from deep ocean warming in climate mitigation scenarios. *Nat. Clim. Change*. **14**, 260–266 (2024).
- Hwang, J. et al. Asymmetric hysteresis response of mid-latitude storm tracks to CO₂ removal. *Nat. Clim. Change*. **14**, 496–503 (2024).
- Liu, C. et al. Hysteresis of the El Niño–Southern oscillation to CO₂ forcing. *Sci. Adv.* **9**, eadh8442 (2023).
- Ehlert, D. & Zickfeld, K. Irreversible ocean thermal expansion under carbon dioxide removal. *Earth Syst. Dyn.* **9**, 197–210 (2018).
- Cao, L., Jin, X.-Y. & Jiang, J. Simulated carbon cycle and Earth system response to atmospheric CO₂ removal. *Adv. Clim. Change Res.* **14**, 313–321 (2023).
- Wu, P., Ridley, J., Pardaens, A., Levine, R. & Lowe, J. The reversibility of CO₂ induced climate change. *Clim. Dyn.* **45**, 745–754 (2015).
- Frölicher, T. L. & Joos, F. Reversible and irreversible impacts of greenhouse gas emissions in multi-century projections with the NCAR global coupled carbon cycle–climate model. *Clim. Dyn.* **35**, 1439–1459 (2010).
- Jeltsch-Thömmes, A., Stocker, T. F. & Joos, F. Hysteresis of the Earth system under positive and negative CO₂ emissions. *Environ. Res. Lett.* **15**, 124026 (2020).
- Walton, J. & Huntingford, C. Little evidence of hysteresis in regional precipitation, when indexed by global temperature rise and fall in an overshoot climate simulation. *Environ. Res. Lett.* **19**, 084028 (2024).
- Siler, N., Roe, G. H., Armour, K. C. & Feldl, N. Revisiting the surface-energy-flux perspective on the sensitivity of global precipitation to climate change. *Clim. Dyn.* **52**, 3983–3995 (2019).
- Allan, R. P. et al. Physically consistent responses of the global atmospheric hydrological cycle in models and observations. *Surv. Geophys.* **35**, 533–552 (2014).
- Wu, P., Christidis, N. & Stott, P. Anthropogenic impact on Earth’s hydrological cycle. *Nat. Clim. Change*. **3**, 807–810 (2013).
- Simmons, A., Willett, K., Jones, P., Thorne, P. & Dee, D. Low-frequency variations in surface atmospheric humidity, temperature, and precipitation: Inferences from reanalyses and monthly gridded observational data sets. *J. Geophys. Res. Atmos.* **115** (2010).
- O’Gorman, P. & Muller, C. J. How closely do changes in surface and column water vapor follow Clausius–Clapeyron scaling in climate change simulations?. *Environ. Res. Lett.* **5**, 025207 (2010).
- Rowell, D. P. & Jones, R. G. Causes and uncertainty of future summer drying over Europe. *Clim. Dyn.* **27**, 281–299 (2006).
- Pendergrass, A. G., Lehner, F., Sanderson, B. M. & Xu, Y. Does extreme precipitation intensity depend on the emissions scenario?. *Geophys. Res. Lett.* **42**, 8767–8774 (2015).

46. Masson-Delmotte, V. P. *IPCC, 2021: Climate Change 2021: The Physical Science Basis. Contribution of Working Group I to the Sixth Assessment Report of the Intergovernmental Panel on Climate Change* (Cambridge University Press, 2021).
47. Lu, J., Vecchi, G. A. & Reichler, T. Expansion of the Hadley cell under global warming. *Geophys. Res. Lett.* **34** (2007).
48. Pfahl, S., O’Gorman, P. A. & Fischer, E. M. Understanding the regional pattern of projected future changes in extreme precipitation. *Nat. Clim. Change*. **7**, 423–427 (2017).
49. Vecchi, G. A. & Soden, B. J. Global warming and the weakening of the tropical circulation. *J. Clim.* **20**, 4316–4340 (2007).
50. Chadwick, R., Boutle, I. & Martin, G. Spatial patterns of precipitation change in CMIP5: Why the rich do not get richer in the tropics. *J. Clim.* **26**, 3803–3822 (2013).
51. Simpson, I. R. et al. Observed humidity trends in dry regions contradict climate models. *Proc. Natl Acad. Sci. USA*. **121**, e2302480120 (2024).
52. Schwinger, J., Asaadi, A., Steinert, N. J. & Lee, H. Emit now, mitigate later? Earth system reversibility under overshoots of different magnitudes and durations. *Earth Syst. Dyn.* **13**, 1641–1665 (2022).
53. Schwinger, J., Asaadi, A., Goris, N. & Lee, H. Possibility for strong northern hemisphere high-latitude cooling under negative emissions. *Nat. Commun.* **13**, 1095 (2022).
54. An, S. I., et al. Global cooling hiatus driven by an AMOC overshoot in a carbon dioxide removal scenario. *Earth’s Future* **9**, e2021EF002165 (2021).
55. Palazzo Corner, S. et al. The zero emissions commitment and climate stabilization. *Front. Sci.* **1**, 1170744 (2023).
56. Previdi, M., Smith, K. L. & Polvani, L. M. Arctic amplification of climate change: a review of underlying mechanisms. *Environ. Res. Lett.* **16**, 093003 (2021).
57. Pfleiderer, P., Schleussner, C.-F. & Sillmann, J. Limited reversal of regional climate signals in overshoot scenarios. *Environ. Res. Clim.* **3**, 015005 (2024).
58. Roldán-Gómez, P. J., De Luca, P., Bernardello, R. & Donat, M. G. Regional irreversibility of mean and extreme surface air temperature and precipitation in CMIP6 overshoot scenarios associated with interhemispheric temperature asymmetries. *Earth Syst. Dyn.* **16**, 1–27 (2025).
59. Douglas, H. C. et al. Drivers of regional variation in the de-emergence of climate change under negative emissions. *J. Clim.* **38**, 1333–1350 (2025).
60. Liu, C. et al. Hemispheric asymmetric response of tropical cyclones to CO₂ emission reduction. *npj Clim. Atmos. Sci.* **7**, 83 (2024).
61. Kim, S.-Y. et al. Hemispherically asymmetric Hadley cell response to CO₂ removal. *Sci. Adv.* **9**, eadg1801 (2023).
62. Frierson, D. M. & Hwang, Y.-T. Extratropical influence on ITCZ shifts in slab ocean simulations of global warming. *J. Clim.* **25**, 720–733 (2012).
63. Donohoe, A., Marshall, J., Ferreira, D. & McGee, D. The relationship between ITCZ location and cross-equatorial atmospheric heat transport: From the seasonal cycle to the Last Glacial Maximum. *J. Clim.* **26**, 3597–3618 (2013).
64. Moreno-Chamarro, E., Marshall, J. & Delworth, T. L. Linking ITCZ migrations to the AMOC and North Atlantic/Pacific SST decadal variability. *J. Clim.* **33**, 893–905 (2020).
65. Oh, H. et al. Contrasting hysteresis behaviors of Northern Hemisphere land monsoon precipitation to CO₂ pathways. *Earth’s Future* **10**, e2021EF002623 (2022).
66. Bischoff, T. & Schneider, T. Energetic constraints on the position of the intertropical convergence zone. *J. Clim.* **27**, 4937–4951 (2014).
67. White, R. et al. Tropical precipitation and cross-equatorial heat transport in response to localized heating: basin and hemisphere dependence. *Geophys. Res. Lett.* **45**, 11,949–911,958 (2018).
68. Marshall, J., Donohoe, A., Ferreira, D. & McGee, D. The ocean’s role in setting the mean position of the Inter-Tropical Convergence Zone. *Clim. Dyn.* **42**, 1967–1979 (2014).
69. Lian, X. et al. Multifaceted characteristics of dryland aridity changes in a warming world. *Nat. Rev. Earth Environ.* **2**, 232–250 (2021).
70. Abel, C. et al. The human–environment nexus and vegetation–rainfall sensitivity in tropical drylands. *Nat. Sustain.* **4**, 25–32 (2021).
71. Middleton, N. & Sternberg, T. Climate hazards in drylands: a review. *Earth-Sci. Rev.* **126**, 48–57 (2013).
72. Danabasoglu, G. et al. The community earth system model version 2 (CESM2). *J. Adv. Model. Earth Syst.* **12**, e2019MS001916 (2020).
73. Smith, R. et al. The parallel ocean program (POP) reference manual: Ocean component of the community climate system model (CCSM). *Rep. LAUR-01853* **141**, 1–141 (2010).
74. Bailey, D. A., Holland, M. M., DuVivier, A. K., Hunke, E. C. & Turner, A. K. Impact of a new sea ice thermodynamic formulation in the CESM2 sea ice component. *J. Adv. Model. Earth Syst.* **12**, e2020MS002154 (2020).
75. Long, M. C., et al. Simulations with the marine biogeochemistry library (MARBL). *J. Adv. Model. Earth Syst.* **13**, e2021MS002647 (2021).
76. Park, S.-W., Noh, K. M., Kug, J.-S. & An, S.-I. How will global carbon cycle respond to negative emissions? *ESS Open Archive* (2023).
77. Harris, I., Osborn, T. J., Jones, P. & Lister, D. Version 4 of the CRU TS monthly high-resolution gridded multivariate climate dataset. *Sci Data* **7**, 109 (2020).
78. Allen, R., Smith, M., Perrier, A. & Pereira, L. S. An update for the definition of reference evapotranspiration. *ICID Bull.* **43**, 1–34 (1994).
79. Begueria, S., Vicente-Serrano, S. M., Reig, F. & Latorre, B. Standardized precipitation evapotranspiration index (SPEI) revisited: parameter fitting, evapotranspiration models, tools, datasets and drought monitoring. *Int. J. Climatol.* **34**, 3001–3023 (2014).
80. Hulme, M. Recent climatic change in the world’s drylands. *Geophys. Res. Lett.* **23**, 61–64 (1996).
81. Park, C.-E. et al. Keeping global warming within 1.5 °C constrains emergence of aridification. *Nat. Clim. Change*. **8**, 70–74 (2018).
82. Middleton, N. & Thomas, D. *World Atlas of Desertification* Arnold (Hodder Headline, PLC, 1997).
83. Hoffmann, R., Abel, G., Malpede, M., Muttarak, R. & Percoco, M. Drought and aridity influence internal migration worldwide. *Nat. Clim. Change*. **14**, 1245–1253 (2024).
84. Berghuijs, W. R. et al. Groundwater recharge is sensitive to changing long-term aridity. *Nat. Clim. Change*. **14**, 357–363 (2024).
85. Benjamini, Y. & Hochberg, Y. Controlling the false discovery rate: a practical and powerful approach to multiple testing. *J. Royal Stat. Soc. Ser. B (Methodol.)* **57**, 289–300 (1995).
86. Wilks, D. “The stippling shows statistically significant grid points”: How research results are routinely overstated and overinterpreted, and what to do about it. *Bull. Am. Meteorol. Soc.* **97**, 2263–2273 (2016).
87. Piao, J. et al. *Zeonodo* <https://doi.org/10.5281/zenodo.15872988> (2025).

Acknowledgements

J.-L.P. was supported by the National Natural Science Foundation of China (Grant 42230605 and 42375044). J.-S.K. was partly supported by the National Research Foundation of Korea (NRF) grant funded by the Korean government (NRF-2022R1A3B1077622) and the Korea Meteorological Administration Research and Development Program under Grant (RS-2025-02222417). W.C. was supported by the Yunnan International Joint Laboratory of Monsoon and Extreme Climate Disasters (Award number 202403AP140009). This work was supported by Institute of Information & communications Technology Planning & Evaluation (IITP) grant funded by the Korea government (MSIT) [NO.RS-2021-1I211343, Artificial Intelligence Graduate School Program (Seoul National University)].

Author contributions

J.L.P. conducted analyses, prepared the figures and wrote the manuscript. W.C. and J.-S.K. designed the research and wrote the paper. S.F.C., J.-H.O., L.W., and Q.Y.C. discussed the results and revised the paper.

Competing interests

The authors declare no competing interests.

Additional information

Supplementary information The online version contains supplementary material available at <https://doi.org/10.1038/s43247-025-02742-y>.

Correspondence and requests for materials should be addressed to Wen Chen or Jong-Seong Kug.

Peer review information *Communications Earth & Environment* thanks Hunter Douglas and the other, anonymous, reviewer(s) for their contribution to the peer review of this work. Primary Handling Editors: Min-Hui Lo, Somaparna Ghosh, Aliénor Lavergne. A peer review file is available.

Reprints and permissions information is available at <http://www.nature.com/reprints>

Publisher's note Springer Nature remains neutral with regard to jurisdictional claims in published maps and institutional affiliations.

Open Access This article is licensed under a Creative Commons Attribution-NonCommercial-NoDerivatives 4.0 International License, which permits any non-commercial use, sharing, distribution and reproduction in any medium or format, as long as you give appropriate credit to the original author(s) and the source, provide a link to the Creative Commons licence, and indicate if you modified the licensed material. You do not have permission under this licence to share adapted material derived from this article or parts of it. The images or other third party material in this article are included in the article's Creative Commons licence, unless indicated otherwise in a credit line to the material. If material is not included in the article's Creative Commons licence and your intended use is not permitted by statutory regulation or exceeds the permitted use, you will need to obtain permission directly from the copyright holder. To view a copy of this licence, visit <http://creativecommons.org/licenses/by-nc-nd/4.0/>.

© The Author(s) 2025